ADVANCES IN ATMOSPHERIC SCIENCES
大气科学进展

The DOI for this manuscript is doi: 10.1007/s00376-017-7028-z.

Modulation of the Aleutian--Icelandic Low Seesaw and Its Surface Impacts by the Atlantic Multidecadal Oscillation

Fei LI [*1,2,3], Yvan J. ORSOLINI[1], Huijun WANG [3,4,2] , Yongqi GAO [5,2], and Shengping HE [6,4,3]

[1]*NILU- Norwegian Institute for Air Research, Kjeller* 2007, *Norway*

[2]*Nansen-Zhu International Research Centre, Institute of Atmospheric Physics, Chinese Academy of Sciences, Beijing* 100029, *China*

[3]*Collaborative Innovation Center on Forecast and Evaluation of Meteorological Disasters/Key Laboratory of Meteorological Disaster, Ministry of Education, Nanjing University of Information Science and Technology, Nanjing* 210044, *China*

[4]*Climate Change Research Center, Chinese Academy of Sciences, Beijing* 100029, *China*

[5]*Nansen Environmental and Remote Sensing Center and Bjerknes Center for Climate Research, Bergen* 5006, *Norway*

[6]*Geophysical Institute, University of Bergen and Bjerknes Center for Climate Research, Bergen* 5007, *Norway*

(Received 1 February 2017; revised 30 May 2017; accepted 22 June 2017)

ABSTRACT

Early studies suggested that the Aleutian--Icelandic low seesaw (AIS) features multidecadal variation. In this study, the multidecadal modulation of the AIS and associated

*Corresponding author: Fei LI

Email: lifei-715@163.com

surface climate by the Atlantic Multidecadal Oscillation (AMO) during late winter (February--March) is explored with observational data. It is shown that, in the cold phase of the AMO (AMO|−), a clear AIS is established, while this is not the case in the warm phase of the AMO (AMO|+). The surface climate over Eurasia is significantly influenced by the AMO's modulation of the Aleutian low (AL). For example, the weak AL in AMO|− displays warmer surface temperatures over the entire Far East and along the Russian Arctic coast and into Northern Europe, but only over the Russian Far East in AMO|+. Similarly, precipitation decreases over central Europe with the weak AL in AMO|−, but decreases over northern Europe and increases over southern Europe in AMO|+.

The mechanism underlying the influence of AMO|− on the AIS can be described as follows: AMO|− weakens the upward component of the Eliassen--Palm flux along the polar waveguide by reducing atmospheric blocking occurrence over the Euro--Atlantic sector, and hence drives an enhanced stratospheric polar vortex. With the intensified polar night jet, the wave trains originating over the central North Pacific can propagate horizontally through North America and extend into the North Atlantic, favoring an eastward-extended Pacific--North America--Atlantic pattern, and resulting in a significant AIS at the surface during late winter.

Key words: Aleutian--Icelandic low seesaw, Atlantic Multidecadal Oscillation, Pacific--North America--Atlantic pattern, stratospheric polar vortex

1. Introduction

During boreal winter, there are two major climatological surface low-pressure cells in the Northern Hemisphere: the Aleutian low (AL) and the Icelandic low (IL). Early studies indicated that the AL and IL vary in an anti-phase seesaw pattern on the interannual timescale, particularly during late winter (February--March) (Honda et al., 2001; Honda and Nakamura, 2001; Orsolini, 2004). Honda et al. (2001) named this pattern the Aleutian and Icelandic low seesaw (AIS). Combining both observations and simulations with an atmospheric general circulation model (AGCM), Honda et al. (2005a) put forward a dynamical pathway for the formation of the AIS, consisting of a three-step process: (1) the AIS starts with the North Pacific variability associated with the AL; (2) the North Pacific influence extends across North America through the eastward propagation of stationary Rossby wave trains, which corresponds to the Pacific--North America (PNA) pattern (Wallace and Gutzler, 1981); and (3) IL anomalies form as part of the Atlantic edge of the PNA-like wave trains. Typically, the formation of the AIS begins with an anomalous AL and ends with the Pacific--North America--Atlantic (PNAA) pattern (Honda et al., 2005b; focused on 1973--1994), as well as upward propagation from the surface into the stratosphere during late winter (Nakamura and Honda, 2002; focus on 1966/67--1996/97). Orsolini et al. (2008) used AGCM simulations to demonstrate that El Niño can extend its influence into the Icelandic sector, forming a PNAA pattern, and into the stratosphere, via the horizontal and vertical propagation of planetary waves modulated by the maturation of the AIS during late winter.

Honda et al. (2005b) showed a significant influence of the AIS on surface air temperature (TS) and precipitation over the extratropical Northern Hemisphere during late

winter, except in central continental regions. The AIS modulates the storm-track activity over both Pacific and Atlantic basins, which produces a downstream increase in eddy activity and precipitation (Garreaud, 2007). However, they also noted that the anti-correlation between the AL and IL is not always significant during the 20th century, but undergoes multidecadal modulations. Sun and Tan (2013) explored the formation of the AIS pattern and attributed it to a stronger stratospheric polar vortex, which may act to reflect the eastern North Pacific wave trains (EPWs) in December--March (focused on 1948--2009). The role of the polar vortex in linking the Aleutian and North Atlantic variability was also noted by Castanheira and Graf (2003).

The Atlantic Multidecadal Oscillation (AMO) is a basin-scale oceanic pattern of sea surface temperature (SST) variability on a multidecadal timescale [~60--70 years (Kerr, 2000)]. Cold AMO phases (AMO|−) occur in the 1900s--1920s and 1970s--1990s, while warm AMO phases (AMO|+) occur in the 1930s--1950s and after the mid-1990s. The fluctuations of the AMO are associated with numerous climatic phenomena. For example, the AMO induces North Atlantic Oscillation (NAO)--like anomalies during late winter (Omrani et al., 2014). Peings and Magnusdottir (2016) also explored the wintertime atmospheric response to the Atlantic multidecadal variability, based on three different configurations of version 5 of the Community Atmosphere Model (low-top, high-top, and low-top coupled to a slab ocean). They suggested different timings of the NAO-like response, which they attributed to an earlier occurrence of the polar warming in the stratosphere in the high-top configuration. Remotely, the AMO modulates the East Asian monsoon through coupled

atmosphere--ocean feedbacks in the western Pacific and Indian oceans (Lu et al., 2006; Li and Bates, 2007). Moreover, AMO|+ increases the frequency of atmospheric blocking highs over the Euro--Atlantic sector by changing the baroclinicity and the transient eddy activity (Häkkinen et al., 2011; Peings and Magnusdottir, 2014). The increased blocking highs over the Euro--Atlantic sector can further enhance upward planetary wave propagation, resulting in stratospheric warming (i.e., a weaker polar vortex) (Nishii et al., 2011).

Despite our incomplete understanding of the connection between the AMO and the stratosphere (Reichler et al., 2012), we try in this study to determine whether the AMO is linked to the multi-decadal variability of the AIS and the associated surface climate during the 20th century using observational/reanalysis data, and whether the potential driver is the AMO's modulation of the stratospheric polar vortex.

2. Data, climatic index and method

We use five monthly mean datasets: (1) sea level pressure (SLP) from HadSLP2r (Allan and Ansell, 2006) during 1860--2016; (2) atmospheric fields from NCEP/NCAR Reanalysis 1 (Kalnay et al., 1996) during 1948--2016; (3) TS from CRU TS3.24 (Harris et al., 2014) during 1901--2015; (4) precipitation from GPCC Reanalysis 7.0 (Schneider et al., 2015) during 1901--2016; and (5) SST from Kaplan Extended SST V2 (Kaplan et al., 1998) during 1856--2017. The analyzed period extends from 1948 to 2011, which allows for atmospheric fields from the relatively reliable NCEP-1 to be used. Besides, our analysis focuses on late winter (February--March), when the AIS is mature and stable (Honda et al., 2001; also see Fig. S2).

The AL and IL indices are defined as the average anomalies of SLP over (50°--60°N, 185°--215°E) and (55°--65°N, 315°--345°E), respectively (Orsolini et al., 2008; derived from HadSLP2r). The AIS index is the difference between the normalized AL and IL indices. A positive value of the AL (AIS) index corresponds to a weak AL (a weak AL and a stronger IL). The AIS index used here differs slightly from the one defined by Honda et al. (2005b). The main difference is the geographical sector used for the AL definition, which in our case is situated farther north, in the region of strongest SLP variance in February. The correlation coefficient between the AIS index used here and that used by Honda et al. (2005b) is 0.94 (over the 99% confidence level) (Fig. S1). The smoothed AMO index is based upon the average SST anomaly (SSTA) in the North Atlantic basin (0°--70°N) during 1861--2011 (available at https://www.esrl.noaa.gov/psd/data/timeseries/AMO/). Weak (strong) AL years are determined when the normalized AL index is above (below) a standard deviation from the mean of 0.8 (−0.8). The AMO|+ and AMO|− phases correspond to cases in which the smoothed AMO index is above and below zero, respectively. The classification of weak and strong AL years according to the different phases of the AMO, used for the composite analysis, is shown in Table 1.

Regarding the statistical methods used in this study, we employ correlation analysis, linear regression, and composite analysis. The statistical significance of correlation is assessed using the two-tailed Student's *t*-test. The wave activity flux (WAF) is used to identify the origin and propagation of Rossby wave--like perturbations, which are calculated in the quasi-geostrophic framework (Plumb, 1985). The Eliassen--Palm (EP) flux (Andrews

et al., 1987) is used to measure the planetary wave (wavenumbers 1--3) activity propagation. Blocking high events are defined as intervals in which daily 500-hPa height from the reanalysis exceeds a standard deviation of 1 above the monthly mean for each grid cell over five consecutive days (Thompson and Wallace, 2001; Liu et al., 2012; Tang et al., 2013). The incidence of blocking highs is measured as (1) the percentage relative to the blocking climatology during 1948--2011 or (2) the ratio of the number of days when a certain grid point is blocked to the total number of days.

3. AIS connection to the AMO

Figure 1a illustrates the time series of the AL and IL indices from 1860 to 2016, February--March. The AL and IL indices have been detrended by removing the long-term linear trend. Year-to-year variations in the AL and IL show an anti-correlation over the 157 years, with a coefficient of −0.26 (over the 99% confidence level). The correlations between the AL and IL indices, computed over a 25-year moving window, are presented in Fig. 1b. The main result is that the AL--IL relationship displays multidecadal non-stationarity. The anti-correlation significance is higher than the 95% confidence level, over the 1900s--1920s and 1970s--1990s approximately. It is statistically insignificant before the 1900s and after the mid-1990s, and even changes sign over the 1930s--1950s. Note that the significant anti-correlation period (the 1970s--1990s) revealed by the present study is in good agreement with the analyzed period (1973--94) in Honda et al. (2001).

Figure 1c illustrates the time series of the smoothed AMO from 1861 to 2011, February--March. Composite analysis of February--March SSTAs between AMO|− and

AMO|+ years (Fig. 1d) shows cold anomalies over the North Atlantic, with a minimum of −0.30°C over the subpolar region, and warm anomalies over the South Atlantic (up to 0.13°C). Interestingly, significant anti-correlations between the AL and IL exist only in AMO|−. The period of AMO|+ shows no significant correlation.

To investigate the effects of AMO phases on the intensity of the AL and IL and on the formation of the AIS, we conduct a composite analysis for the whole period, as well as for each phase of the AMO. The upper panel of Fig. 2 illustrates the composite differences of February--March SLP (derived from HadSLP2r) between weak and strong AL years for 1861--2011, as well as in AMO|+ and AMO|−. For the whole period, the weak AL is associated with positive SLP anomalies over the North Pacific, and negative SLP anomalies over the polar cap and Iceland (Fig. 2a). In AMO|+, the negative SLP anomalies retreat to the polar cap and even change to positive sign over the Barents Sea (Fig. 2b). There is no AL--IL correlation. In AMO|−, the negative SLP anomalies occupy the polar cap and subpolar North Atlantic, with the minimum located in the climatological center of the IL (Fig. 2c). A clear AIS pattern appears. The same conclusion is reached when using NCEP-1 (1948--2011) (Figs. 2d--f) instead of HadSLP2r.

The upper panel of Fig. 3 illustrates the composite differences of February--March 250-hPa geopotential height (Z250) and horizontal WAF (departures from zonal means) between weak and strong AL years for 1948--2011, as well as in AMO|+ and AMO|−. In the following analysis, our description particularly focuses on the composites for AMO|+ and AMO|−. In AMO|+, the weak AL is associated with positive Z250 anomalies over the North

Pacific and southern United States, and there is a negative Z250 center in central Canada (Fig. 3b). Meanwhile, the PNA-like stationary Rossby wave trains originate over the central North Pacific and stretch horizontally across North America. In AMO|−, the negative Z250 center in central Canada extends considerably farther across Newfoundland, past the south of Greenland (i.e., the subpolar North Atlantic; Fig. 3c), as another wave train emanates from the leading edge of the PNA-like Rossby wave to form the PNAA pattern (Honda et al., 2001, 2005a). This pattern is analogous to the EPWs in Sun and Tan (2013), which originate over the central North Pacific and propagate horizontally through North America and into the North Atlantic.

The lower panel of Fig. 3 is the same as the upper panel, but for zonally averaged zonal wind. In AMO|+, anomalous westward flow is significant along the midlatitudes (30°--40°N) from the surface into the lower stratosphere (Fig. 3e). However, in AMO|−, both anomalous westward and eastward flows are significant, and of stronger magnitude, along the midlatitudes (30°--40°N) and high latitudes (north of 50°N), respectively, from the surface into the upper stratosphere (Fig. 3f), suggesting a stronger stratospheric polar vortex. Thus, the clear AIS seen in the SLP in AMO|− is strongly coupled with the PNAA pattern and EPWs in the upper troposphere, and the stronger stratospheric polar vortex; whereas, in AMO|+, there is no established AIS with the upper-tropospheric PNA pattern.

4. AIS-based surface climate

We extend our investigation into how the AL's impact on surface climate is influenced by the AMO phase. Figure 4 illustrates the composite differences of February--March TS and

1000-hPa horizontal temperature advection between weak and strong AL years for 1948--2011, as well as in AMO|+ and AMO|−. In AMO|+, the weak AL-related anticyclonic anomalies induce cold advection along the west coast of North America and warm advection along the Russian Far East coast; anticyclonic anomalies over the Barents Sea contribute to cold advection over Europe (Fig. 4e). Cold anomalies are pronounced over Canada and Europe (Fig. 4b). In AMO|−, cold anomalies over Canada are much weaker, and warm anomalies extend over the entire Far East and along the Russian Arctic coast (Fig. 4c). Besides, the intensified IL-related cyclonic anomalies (Fig. 4f) lead to cold anomalies over the Middle East, and warm anomalies over northern Europe stretching along the Russian Arctic coast.

Figure 5 is the same as Fig. 4, but for precipitation and 300-hPa zonal wind (U300)/variance of bandpass-filtered (3--7 days) 300-hPa meridional wind (V300). The monthly variance of V300 is calculated from daily mean values, which are then band-pass filtered (3--7 days), to reflect the transient eddy activity. In AMO|+, positive band-passed U300 anomalies occur over the Bering Sea/Aleutian Islands and the United States, and negative band-passed U300 anomalies over the midlatitude North Pacific and Arctic Canada/Europe (Fig. 5e, contours), favoring enhanced (diminished) eddy activity downstream (Fig. 5e, vectors). Correspondingly, positive precipitation anomalies are over western Canada, and negative precipitation anomalies over the western United States and northern Europe (Fig. 5b). In AMO|−, the positive band-passed U300 anomalies over the United States extend eastwards through the North Atlantic, with opposite band-passed U300

anomalies over the Mediterranean Sea, which corresponds to diminished eddy activity and precipitation over southern Europe (Figs. 5c and f).

5. How does the AMO modulate the AIS?

How can the AMO be linked to the AIS multidecadal fluctuations through an anomalous stratospheric polar vortex? To answer this, the composite-differences of daily geopotential height averaged north of 60°N (pressure versus time) between AMO|− and AMO|+ years are presented in Fig. 6a. The subpolar North Atlantic cold SSTAs (see Fig. 1d) are associated with a precursory strengthening of the stratospheric polar vortex during early winter (November--January), which propagates downwards into the troposphere during late winter (February--March). The strengthening of the stratospheric polar vortex (i.e., stratospheric cooling) is mainly maintained by anomalous negative quasi-stationary eddy heat flux (Fig. 6b).

Figure 7 illustrates the composite differences of November--January 20-hPa geopotential height (Z20) and February--March Z250/horizontal WAF (departures from zonal means) between AMO|− and AMO|+ years. The Z20 pattern related to AMO|− shows negative anomalies over the polar cap and positive anomalies in the midlatitudes (Fig. 7a), suggesting an enhanced stratospheric polar vortex during early winter, consistent with Omrani et al. (2014). The negative Z20 anomalies in the Arctic extend downwards to 250 hPa during late winter, accompanied by EPWs that emanate over the eastern North Pacific and stretch horizontally through the western North America--North Atlantic--Europe sector (Fig. 7b).

The composite differences of November--January and February--March EP flux cross sections and zonally averaged zonal wind between AMO|+ and AMO|− years are presented in Figs. 8a and b, respectively. In AMO|−, during early winter, the polar night jet accelerates (Fig. 8a, contours) because of anomalous equatorward-pointing EP flux in the uppermost stratosphere (20 hPa), and anomalous downward-pointing EP flux along the polar waveguide (Dickinson, 1968; Fig. 8a, vectors). During late winter, the anomalous upper-stratospheric equatorward-pointing EP flux disappears, while the anomalous downward-pointing EP flux is stronger in magnitude, moving directly from the upper stratosphere in the high latitudes to reach the surface (Fig. 8b, vectors). The high-latitude zonal wind anomaly strengthens not only in the stratosphere but also in the troposphere (Fig. 8b, contours).

To better understand the spatial modulation of planetary waves associated with the anomalous downward-pointing EP flux at different levels, we calculate the February--March 50-hPa and 250-hPa vertical WAFs in the climatology and the composite difference between AMO|− and AMO|+ years (Figs. 8c and d). The positive (negative) contours represent the upward (downward) climatological stationary wave activity (Plumb, 1985). At 50 hPa, the anomalous downward stationary wave flux over the subpolar North Atlantic related to AMO|− (Fig. 8c, shaded) collocates with the climatological negative center (Fig. 8c, contours). This center of anomalous downward flux is also apparent over northeastern North America and Greenland at 250 hPa (Fig. 8d, shaded), and may superimpose on the horizontal EPWs (Fig. 7b), contributing to an eastward-extended PNAA pattern and the formation of the AIS (Sun and Tan, 2013).

The results mentioned above indicate that the AMO|− phase has the potential to drive an intensified polar night jet because of anomalous downward-pointing EP flux along the polar waveguide (Figs. 8a and b) or, equivalently, because of the negative quasi-stationary eddy heat flux anomalies in the high latitudes (Fig. 6b). It is suggested that the EPWs propagate zonally along the intensified polar night jet in late winter (Fig. 7b). The central question remains as to why AMO|− is associated with an intensified polar vortex, and the answer can be found in how the AMO modulates the occurrence of atmospheric blockings over the Atlantic (Häkkinen et al., 2011; Peings and Magnusdottir, 2014). Reduced occurrence of blocking highs over the Euro--Atlantic sector would imply a lessening of the upward wave activity flux, resulting in a stronger stratospheric polar vortex (Nishii et al., 2011).

To test this, we re-examine the composite differences of the incidence of November--March, November--January and February--March blockings highs (measured as the percentage relative to the blocking climatology during 1948--2011) between AMO|− and AMO|+ years (Fig. 9, left panel). In AMO|−, in early winter, the frequency of blocking highs decreases over the subpolar North Atlantic, while it increases in southern Europe (Fig. 9b). During late winter, the reduced blocking highs are of stronger magnitude over most parts of the Euro--Atlantic sector, except the midlatitude North Atlantic where increased blocking highs are found (Fig. 9c). Figure 9d further confirms that the frequency of blocking highs over the Euro--Atlantic sector (40°--80°N, 85°W--30°E) is lower in AMO|− compared to in AMO|+, especially during late winter. These findings on the occurrence of blockings are in

agreement with Peings and Magnusdottir (2014), and support the association of AMO|− with a strengthened stratospheric vortex.

6. Discussion and conclusions

The present study, based on observations, shows:

(1) The significant anti-correlation between the AL and IL in February--March is not a consistent feature during the 20th century, and emerges only in AMO|−. The AIS is clearly established and is strongly coupled with the PNAA pattern and EPWs in the upper troposphere, and the intensified polar night jet. On the contrary, in AMO|+ occurs, the AIS is not established, featuring the upper-tropospheric PNA pattern only.

(2) The surface climate over Eurasia is sensitive to the establishment of the AIS. With an established AIS (weak AL and strong IL), the Middle East (Far East) is colder (warmer) than normal, and southern Europe experiences less rain. However, without an established AIS (weak AL only), Europe (the Russian Far East) is colder (warmer) than normal, and northern Europe receives less rain.

(3) The AMO|− phase favors a clear AIS mainly because of its influence on the intensified polar night jet, via weakening the EP flux along the polar waveguide/negative quasi-stationary eddy heat flux anomalies in the high latitudes, which can be achieved by atmospheric blocking modulation (Häkkinen et al., 2011; Peings and Magnusdottir, 2014; see also Fig. 9). The EPWs propagate zonally along the intensified polar night jet during late winter, favoring an eastward-extended PNAA pattern and resulting in a significant AIS at the surface.

It is important to note that, within a decadal period of AMO|−, the interannually varying AIS can be of either phase, with a concomitant weak or strong AL and an out-of-phase IL. By itself, AMO|− would favor a strong stratospheric polar vortex and IL (Omrani et al., 2014). Hence, the AMO may modulate the stratospheric polar vortex and IL superimposed on the active AIS. In this paper, we select the AMO phases based on the smoothed AMO index above and below zero, and hence the modulation of IL intensity is much weaker (Fig. 7c) compared to the results in Omrani et al. (2014).

In addition, the AIS' connection to different phases of the AMO and to the winter surface climate over Eurasia warrants a study using an AGCM externally forced with observed SST and extending into the stratosphere. This issue will be addressed in future work.

Acknowledgements. The authors are supported by the Research Council of Norway (Grant Nos. EPOCASA #229774/E10 and SNOWGLACE #244166), the National Natural Science Foundation of China (Grant No. 41605059), and the Young Talent Support Plan launched by the China Association for Science and Technology (Grant No. 2016QNRC001).

REFERENCES

Allan, R., and T. Ansell, 2006: A new globally complete monthly historical gridded mean sea level pressure dataset (HadSLP2): 1850-2004. *J. Climate*, **19**, 5816--5842, doi: 10.1175/JCLI3937.1.

Andrews, D. G., 1987: On the interpretation of the eliassen-palm flux divergence. *Quart. J. Roy. Meteor. Soc.*, **113**(475), 323--338, doi: 10.1002/qj.49711347518.

Castanheira, J. M., and H.-F. Graf, 2003: North Pacific-North Atlantic relationships under stratospheric control? *J. Geophys. Res.*, **108**, ACL 11-1--ACL 11-10, doi: 10.1029/2002JD002754.

Dickinson, R. E., 1968: Planetary Rossby waves propagating vertically through weak westerly wind wave guides. *J. Atmos. Sci.*, **25**, 984--1002, doi: 10.1175/1520-0469(1968)025<0984:PRWPVT>2.0.CO;2.

Garreaud, R. D., 2007: Precipitation and circulation covariability in the extratropics. *J. Climate*, **20**(18), 4789--4797, doi: 10.1175/JCLI4257.1.

Häkkinen, S., P. B. Rhines, and D. L. Worthen, 2011: Atmospheric blocking and Atlantic Multidecadal Ocean variability. *Science*, **334**, 655--659, doi: 10.1126/science.1205683.

Harris, I., P. D. Jones, T. J. Osborn, and D. H. Lister, 2014: Updated high-resolution grids of monthly climatic observations-the CRU TS3.10 Dataset. *International Journal of Climatology*, **34**(3), 623--642, doi: 10.1002/joc.3711.

Honda, M., and H. Nakamura, 2001: Interannual seesaw between the Aleutian and Icelandic lows. Part II: Its significance in the interannual variability over the wintertime Northern Hemisphere. *J. Climate*, **14**, 4512--4529, doi: 10.1175/1520-0442(2001)014<4512:ISBTAA>2.0.CO;2.

Honda, M., H. Nakamura, J. Ukita, I. Kousaka, and K. Takeuchi, 2001: Interannual seesaw between the Aleutian and Icelandic lows. Part I: Seasonal dependence and life cycle. *J. Climate*, **14**, 1029--1042, doi: 10.1175/1520-0442(2001)014<1029:ISBTAA>2.0.CO;2.

Honda, M., Y. Kushnir, H. Nakamura, S. Yamane, and S. E. Zebiak, 2005a: Formation, mechanisms, and predictability of the Aleutian-Icelandic low seesaw in ensemble AGCM simulations. *J. Climate*, **18**, 1423--1434, doi: 10.1175/JCLI3353.1.

Honda, M., S. Yamane, and H. Nakamura, 2005b: Impacts of the Aleutian-Icelandic low seesaw on surface climate during the twentieth century. *J. Climate*, **18**(14), 2793--2802, doi: 10.1175/JCLI3419.1.

Kalnay, E., and Coauthors, 1996: The NCEP/NCAR 40-year reanalysis project. *Bull. Amer. Meteor. Soc.*, **77**, 437--471, doi: 10.1175/1520-0477(1996)077<0437:TNYRP>2.0.CO;2.

Kaplan, A., M. A. Cane, Y. Kushnir, A. C. Clement, M. B. Blumenthal, and B. Rajagopalan, 1998: Analyses of global sea surface temperature 1856-1991. *J. Geophys. Res.*, **103**, 18 567--18 589, doi: 10.1029/97JC01736.

Kerr, R. A., 2000: A North Atlantic climate pacemaker for the centuries. *Science*, **288**, 1984--1986, doi: 10.1126/science.288.5473.1984.

Li, S. L., and G. T. Bates, 2007: Influence of the Atlantic multidecadal oscillation on the winter climate of East China. *Adv. Atmos. Sci.*, **24**(1), 126--135, doi: 10.1007/s00376-007-0126-6.

Liu, J., J. A. Curry, H. Wang, M. Song, and R. M. Horton, 2012: Impact of declining Arctic sea ice on winter snowfall. *Proceedings of the National Academy of Sciences of the United States of America*, **109**, 4074--4079, doi: 10.1073/pnas.1114910109.

Lu, R. Y., B. W. Dong, and H. Ding, 2006: Impact of the Atlantic Multidecadal Oscillation on the Asian summer monsoon. *Geophys. Res. Lett.*, **33**(24), doi: 10.1029/2006GL027655.

Nakamura, H., and M. Honda, 2002: Interannual seesaw between the Aleutian and Icelandic lows Part III: Its influence upon the stratospheric variability. *J. Meteor. Soc. Japan*, **80**(4B), 1051--1067, doi: 10.2151/jmsj.80.1051.

Nishii, K., H. Nakamura, and Y. J. Orsolini, 2011: Geographical dependence observed in blocking high influence on the stratospheric variability through enhancement and suppression of upward planetary-wave propagation. *J. Climate*, **24**(24), 6408--6423, doi: 10.1175/JCLI-D-10-05021.1.

Omrani, N.-E., N. S. Keenlyside, J. Bader, and E. Manzini, 2014: Stratosphere key for wintertime atmospheric response to warm Atlantic decadal conditions. *Climate Dyn.*, **42**, 649--663, doi: 10.1007/s00382-013-1860-3.

Orsolini, Y. J., 2004: Seesaw fluctuations in ozone between the North Pacific and North Atlantic. *J. Meteor. Soc. Japan*, **82**(3), 941--949, doi: 10.2151/jmsj.2004.941.

Orsolini, Y. J., N. G. Kvamstø, I. T. Kindem, M. Honda, and H. Nakamura, 2008: Influence of the Aleutian-Icelandic low seesaw and ENSO onto the Stratosphere in ensemble winter hindcasts. *J. Meteor. Soc. Japan*, **86**(5), 817--825, doi: 10.2151/jmsj.86.817.

Peings, Y., and G. Magnusdottir, 2014: Forcing of the wintertime atmospheric circulation by the multidecadal fluctuations of the North Atlantic ocean. *Environmental Research Letters*, **9**(3), 034018, doi: 10.1088/1748-9326/9/3/034018.

Peings, Y., and G. Magnusdottir, 2016: Wintertime atmospheric response to Atlantic multidecadal variability: Effect of stratospheric representation and ocean-atmosphere coupling. *Climate Dyn.*, **47**, 1029--1047, doi: 10.1007/s00382-015-2887-4.

Plumb, R. A., 1985: On the three-dimensional propagation of stationary waves. *J. Atmos. Sci.*, **42**, 217--229, doi: 10.1175/1520-0469(1985)042<0217:OTTDPO>2.0.CO;2.

Reichler, T., J. Kim, E. Manzini, and J. Kröger, 2012: A stratospheric connection to Atlantic climate variability. *Nature Geoscience*, **5**(11), 783--787, doi: 10.1038/ngeo1586.

Schneider, U., A. Becker, P. Finger, A. Meyer-Christoffer, B. Rudolf, and M. Ziese, 2015: GPCC Full Data Reanalysis Version 7.0 at 1.0°: Monthly Land-Surface Precipitation from Rain-Gauges built on GTS based and Historic Data, doi: 10.5065/D6000072.

Sun, J., and B. Tan, 2013: Mechanism of the wintertime Aleutian low-Icelandic low seesaw. *Geophys. Res. Lett.*, **40**(15), 4103--4108, doi: 10.1002/grl.50770.

Tang, Q. H., X. J. Zhang, X. H. Yang, and J. A. Francis, 2013: Cold winter extremes in northern continents linked to Arctic sea ice loss. *Environmental Research Letters*, **8**(1), 014036, doi: 10.1088/1748-9326/8/1/014036.

Thompson, D. W. J, and J. M. Wallace, 2001: Regional climate impacts of the Northern Hemisphere annular mode. *Science*, **293**(5527), 85--89, doi: 10.1126/science.1058958.

Wallace, J. M., and D. S. Gutzler, 1981: Teleconnections in the geopotential height field during the Northern Hemisphere winter. *Monthly Weather Review*, **109**(4), 784--812, https://doi.org/10.1175/1520-0493(1981)109<0784:TITGHF>2.0.CO;2

Table 1. Classification of weak and strong AL years in AMO|+ and AMO|−.

Weak AL	AMO|+	1866, 1876, 1887, 1890, 1892, 1893, 1937, 1944, 1948, 1951, 1955, 1956, 1962, 2006, 2007, 2009, 2011
Strong AL		1861, 1871, 1878, 1879, 1881, 1889, 1898, 1931, 1934, 1941, 1946, 1998, 1999, 2000, 2004, 2010
Weak AL	AMO|−	1903, 1904, 1916, 1918, 1920, 1922, 1923, 1967, 1972, 1982, 1985, 1989, 1995, 1996
Strong AL		1901, 1905, 1908, 1911, 1919, 1926, 1927, 1970, 1977, 1978, 1980, 1981, 1983, 1984, 1986, 1988, 1993

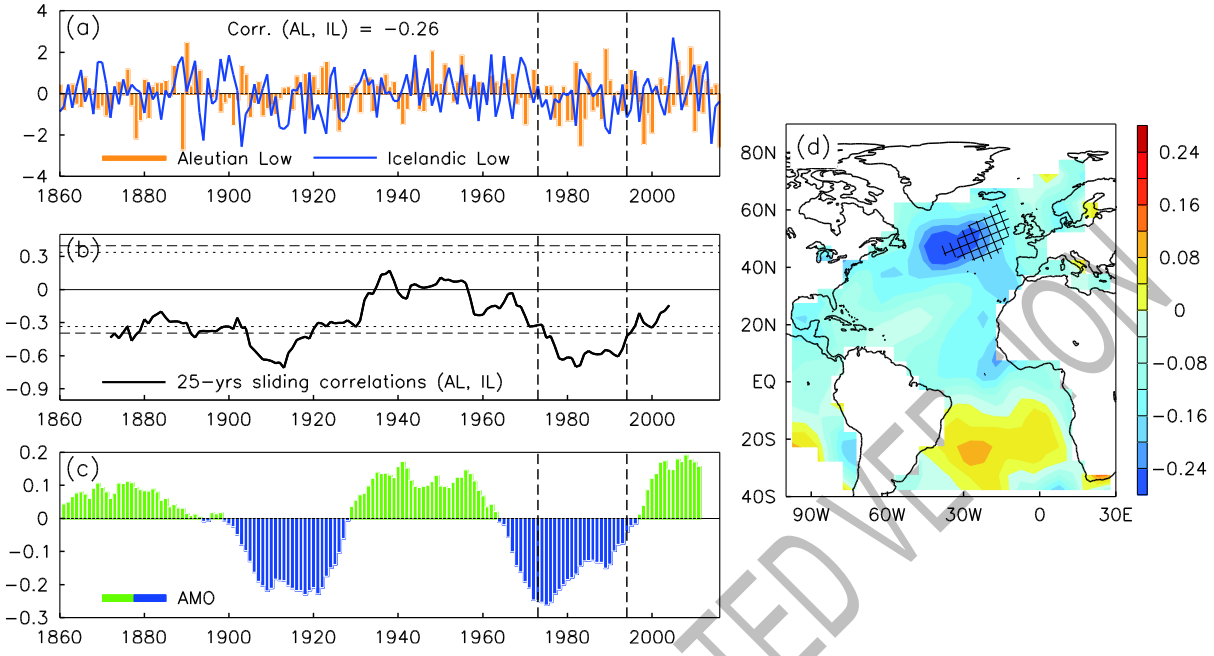

Fig. 1. (a) The AL (orange bars) and IL (blue line) indices from 1860 to 2016, February--March. (b) Correlations in a 25-year moving window between the AL and IL indices. The 90% and 95% confidence level for the correlations is indicated by the horizontal dashed lines. (c) Smoothed AMO index from 1861 to 2011, February--March. The vertical dashed lines reflect the analyzed period (1973--94) in Honda et al. (2001). (d) Composite differences of February--March SST (units: °C) restricted to the Atlantic region between AMO|− and AMO|+ years. Crosshatched region is statistically significant at the 95% confidence level.

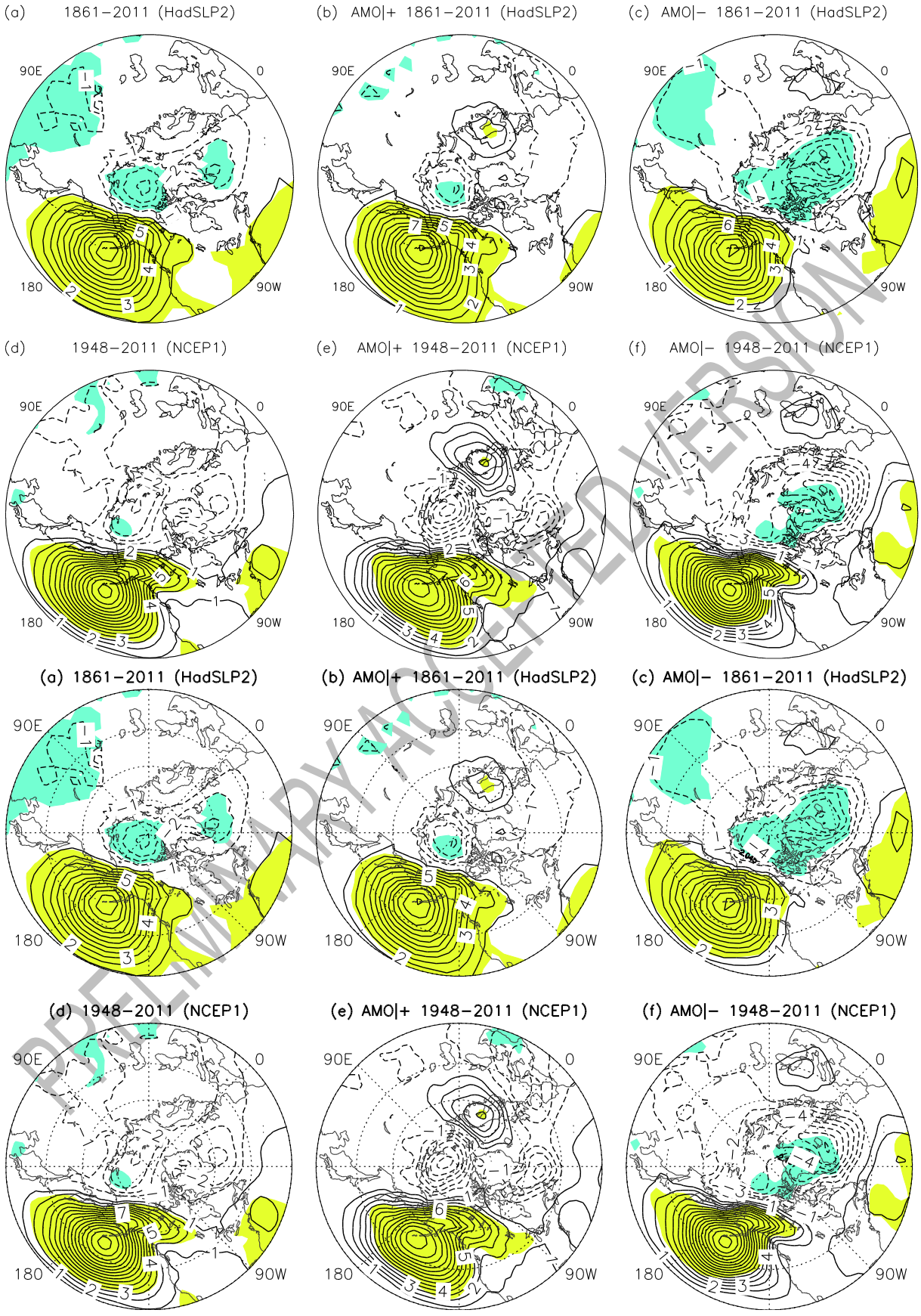

(a) 1861–2011 (HadSLP2)
(b) AMO|+ 1861–2011 (HadSLP2)
(c) AMO|– 1861–2011 (HadSLP2)
(d) 1948–2011 (NCEP1)
(e) AMO|+ 1948–2011 (NCEP1)
(f) AMO|– 1948–2011 (NCEP1)

Fig. 2. Composite differences of February--March SLP (units: hPa) (derived from HadSLP2r) between weak and strong AL years for (a) 1861--2011, and for (b) AMO|+ and (c) AMO|−. (d--f) As in (a--c), but for SLP (derived from NCEP-1, 1948--2011). Shaded regions indicate significance at the 95% confidence level.

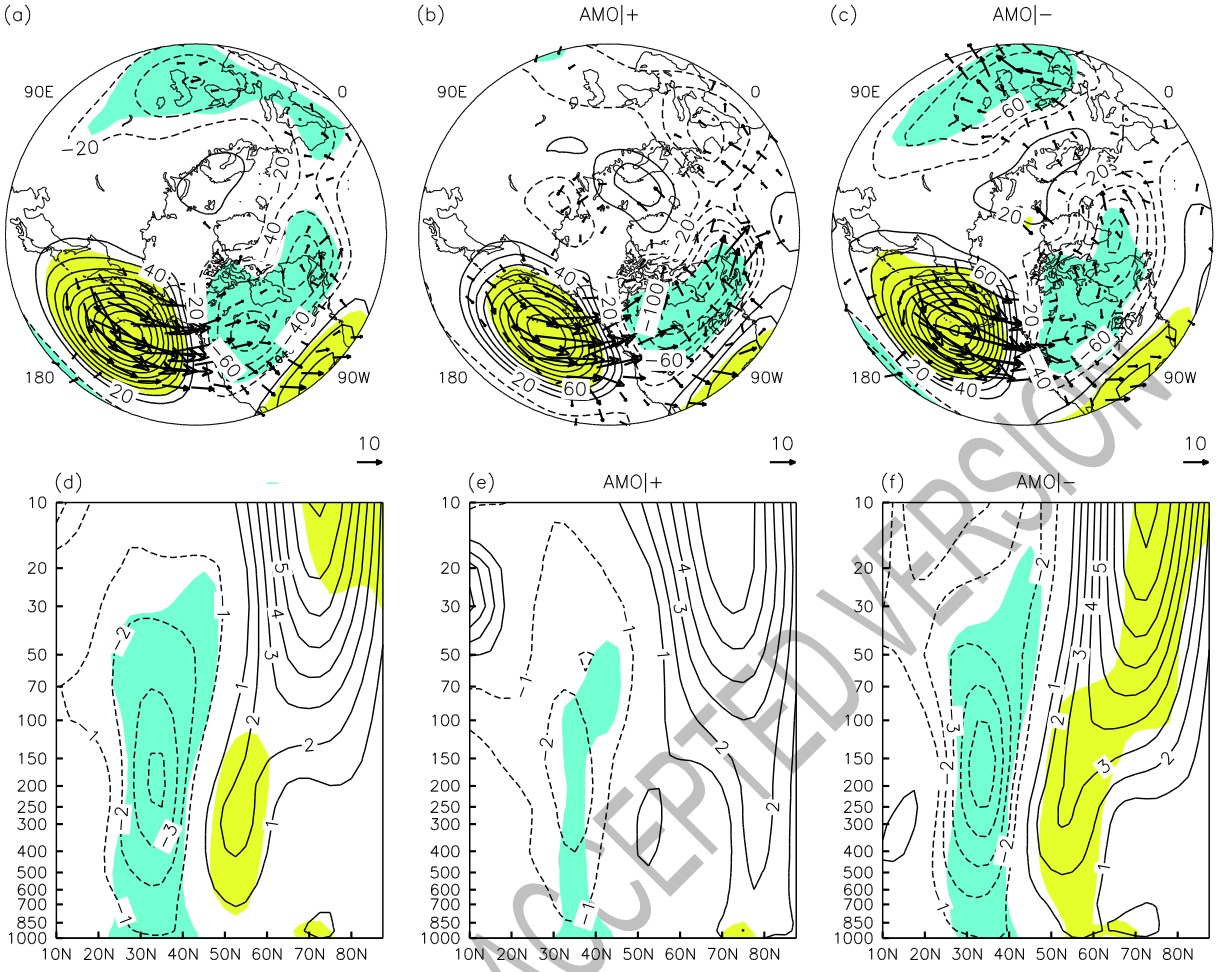

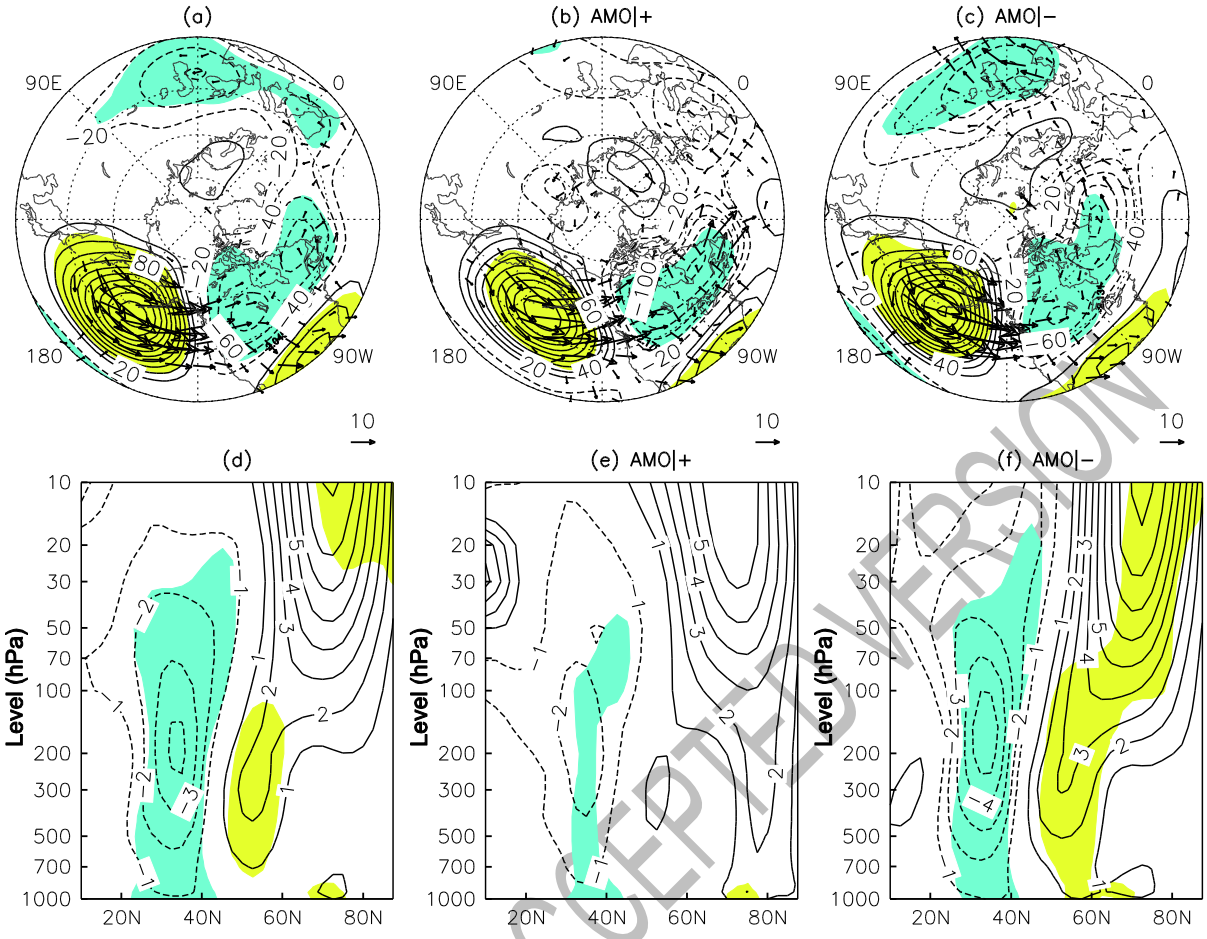

Fig. 3. Composite differences of February--March Z250 (contours; units: gpm)/horizontal WAF (vectors; scale in $m^2\ s^{-1}$) (departures from zonal means) between weak and strong AL years for (a) 1948--2011, and for (b) AMO|+ and (c) AMO|−. (d--f) As in (a-c), but for zonally averaged zonal wind (units: $m\ s^{-1}$). Shaded regions indicate significance at the 95% confidence level.

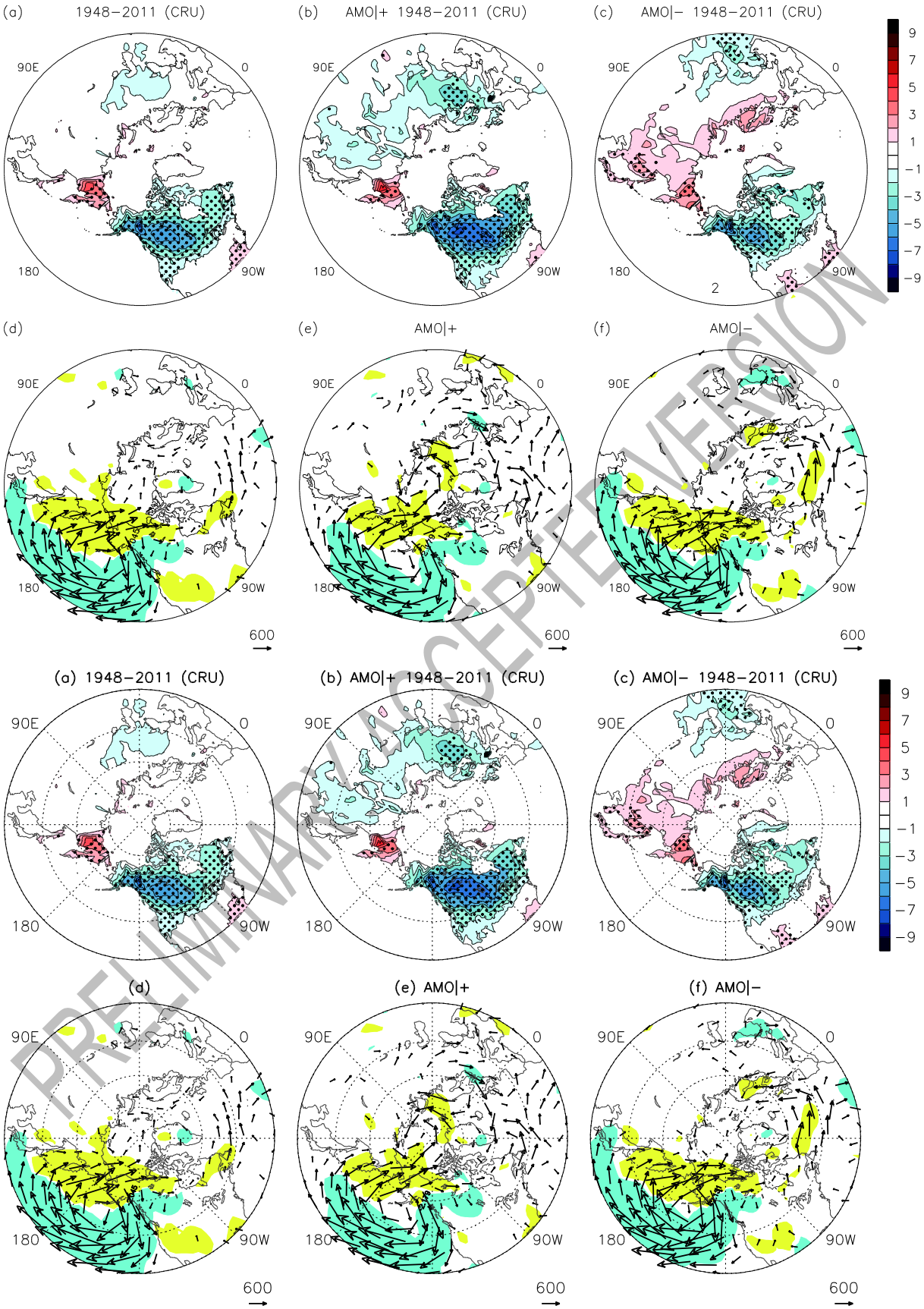

Fig. 4. Composite differences of February--March TS (units: °C) (derived from CRU) between weak and strong AL years for (a) 1948-2011, and for (b) AMO|+, and (c) AMO|−. (d--f) As in (a--c), but for 1000-hPa horizontal temperature advection (scale in m K s^{-1}). Dotted (a--c) and shaded (d--f) regions indicate significance at the 95% confidence level.

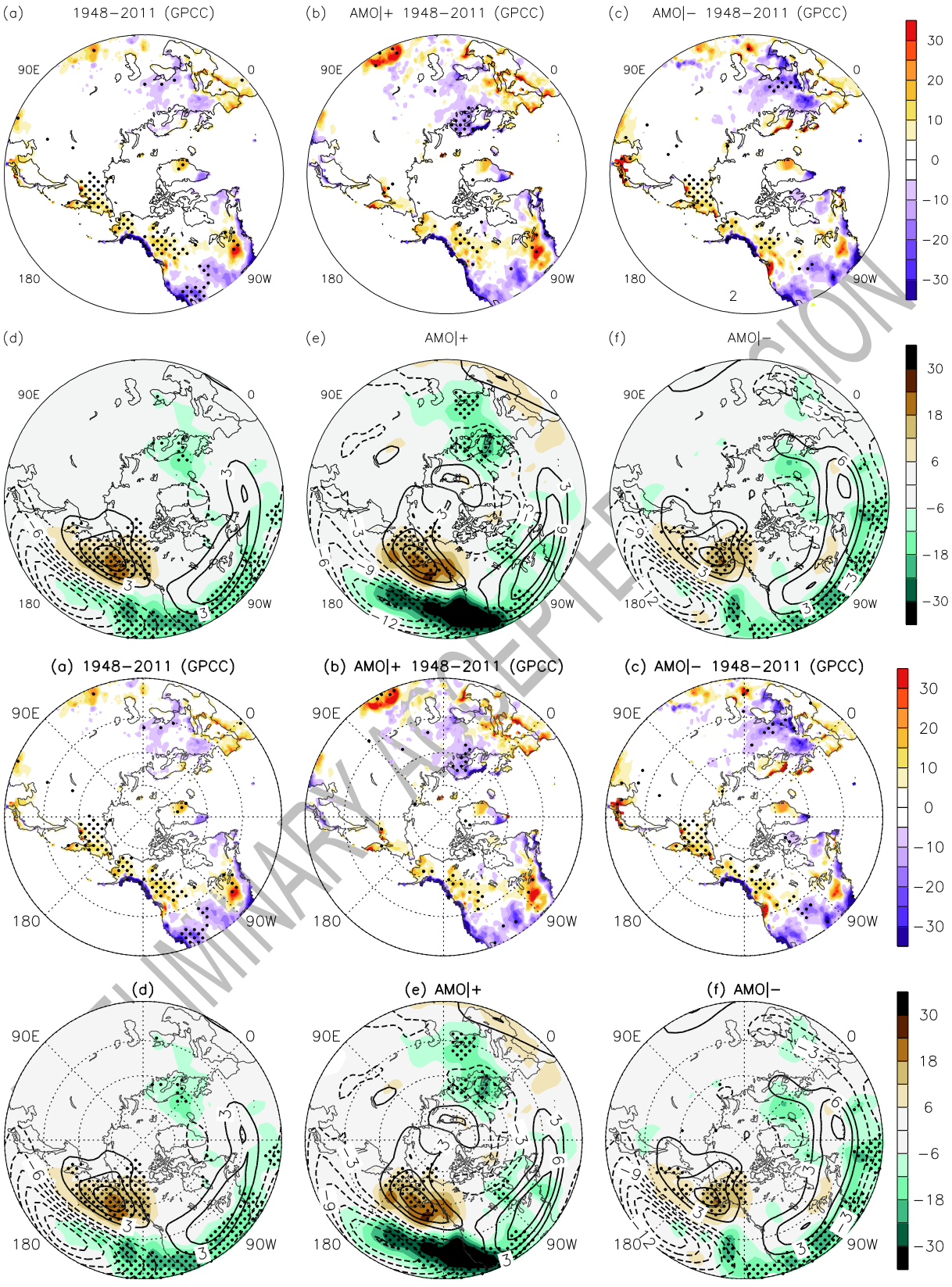

Fig. 5. Composite differences of February--March precipitation (units: mm) (derived from GPCC) between weak and strong AL years for (a) 1948--2011, and for (b) AMO|+ and (c)

AMO|−. (d--f) As in (a--c), but for U300 (contours; unit: m s^{-1})/variance of bandpass-filtered (3--7 days) V300 (shaded, units: m^2 s^{-1}). Dotted regions indicate significance at the 95% confidence level.

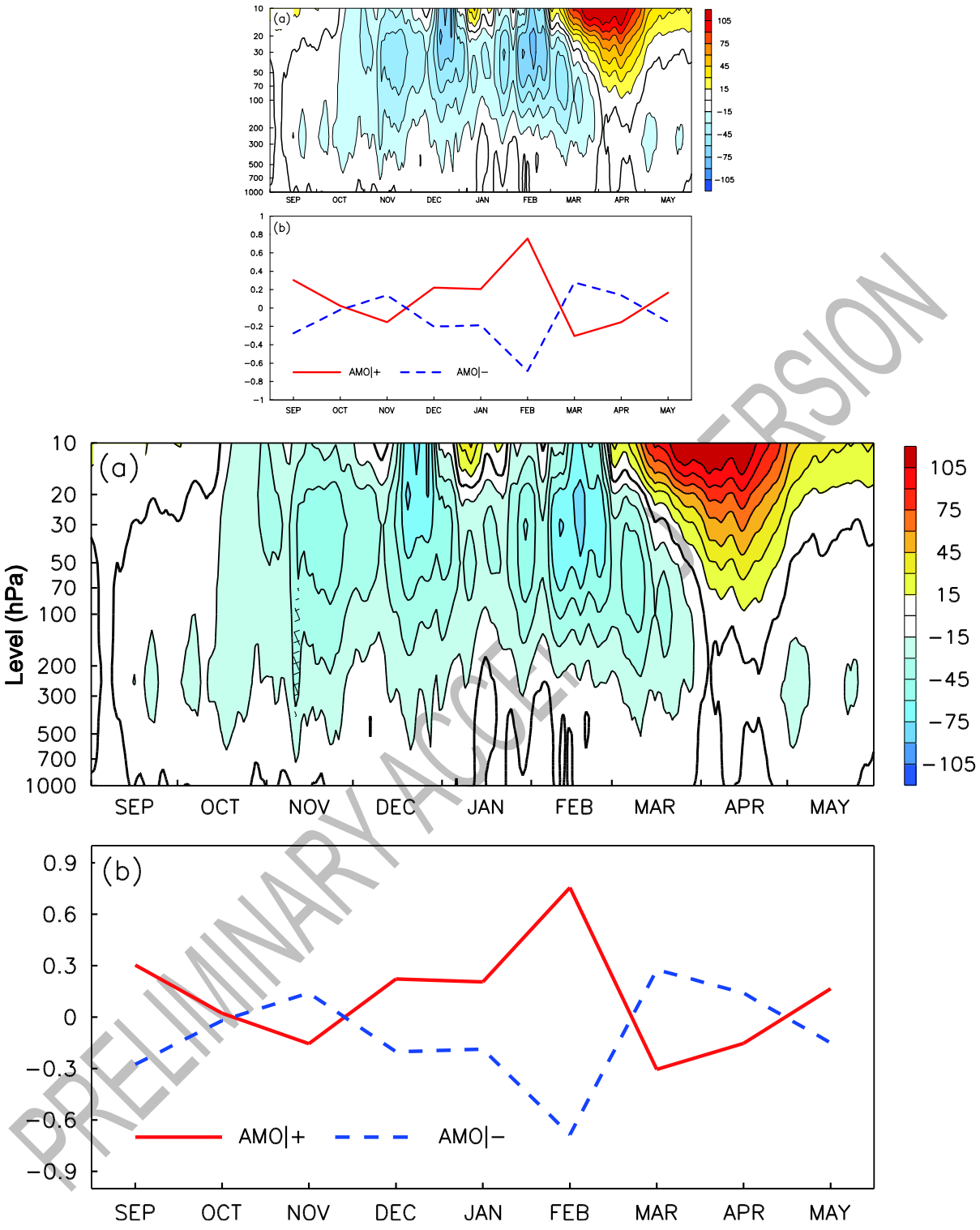

Fig. 6. (a) Temporal evolution of daily geopotential height (units: gpm) averaged north of 60°N for the composite difference between AMO|− and AMO|+ years. (b) Temporal evolution of monthly quasi-stationary eddy heat flux (units: °C m s^{-1}) averaged north of 60°N in the

lowermost stratosphere (150 hPa) for the composite difference with both AMO|+ (red line) and AMO|− (blue line) years.

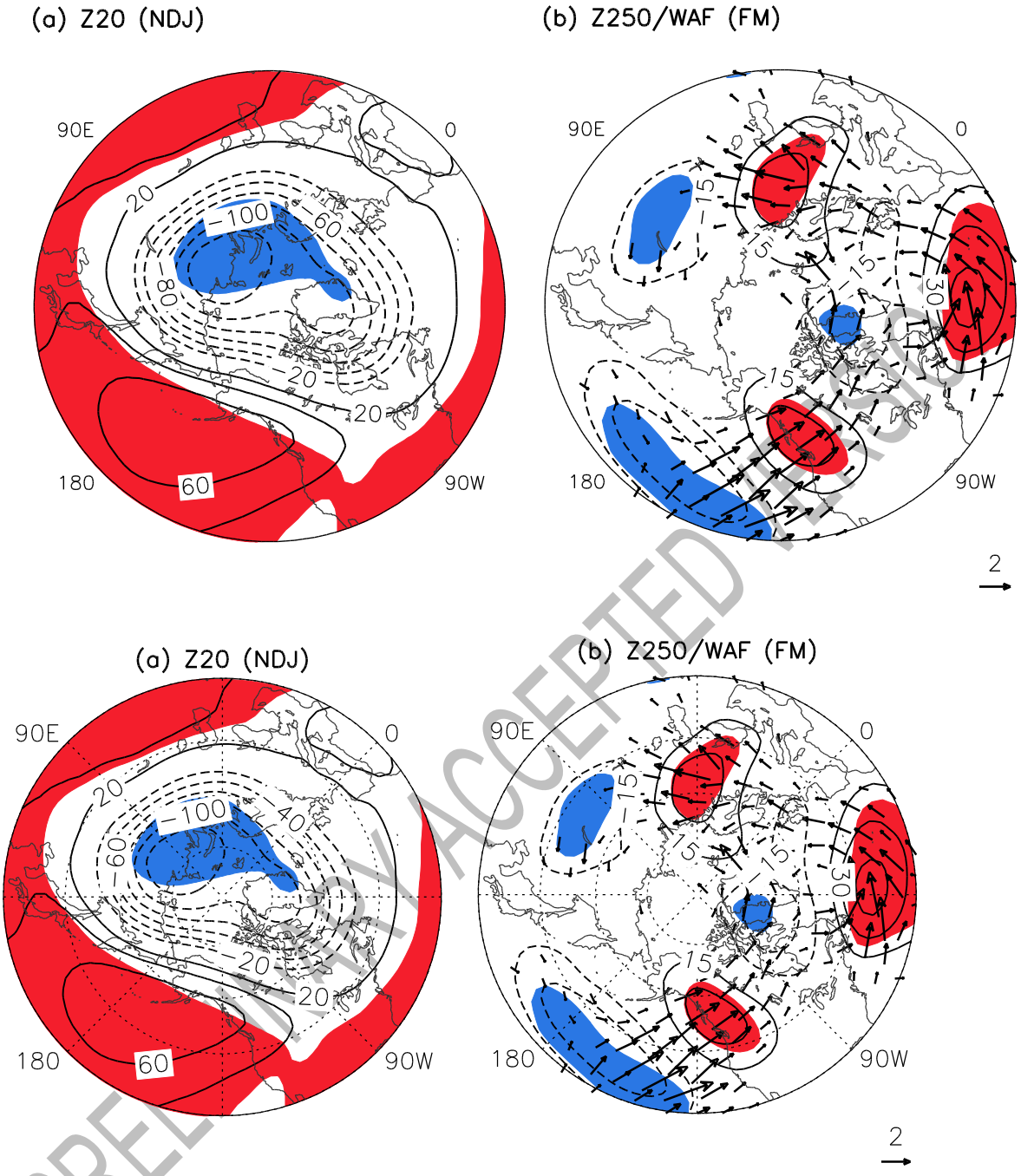

Fig. 7. Composite differences between AMO|− and AMO|+ years of (a) November--January Z20 (units: gpm) and (b) February--March Z250 (contours; units: gpm)/WAF (vectors; scale in $m^2\ s^{-1}$; departures from zonal means) . Shaded regions indicate significance at the 95% confidence level.

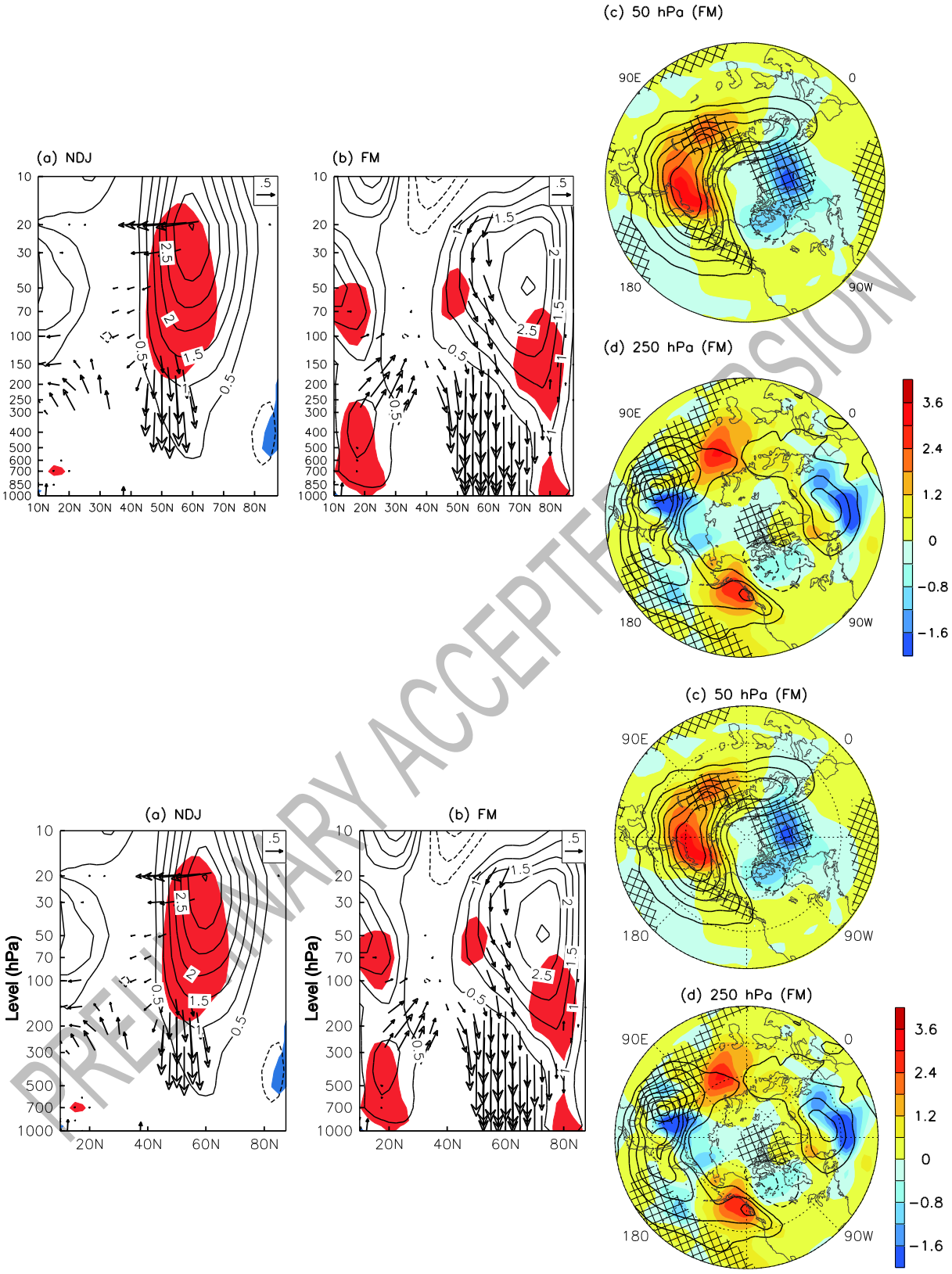

Fig. 8. Composite differences between AMO|− and AMO|+ years of (a) November--January and (b) February--March EP flux cross sections (vectors; scale in $m^2\ s^{-2}$) and zonally averaged

zonal wind (contours; units: m s^{-1}) . Shaded regions indicate significance at the 95% confidence level. In order to display the EP flux throughout the stratosphere, the vectors are scaled by $\sqrt{1000/p}$ and the inverse of air density. Additionally, the vertical component is multiplied by 125. February--March (c) 50-hPa and (d) 250-hPa vertical stationary WAFs in the climatology (1948--2011; contours; unit :10^3 m^2 s^{-2}) and the composite difference between AMO|− and AMO|+ years (shaded; units: 10^3 m^2 s^{-2}). Crosshatched regions indicate significance at the 95% confidence level.

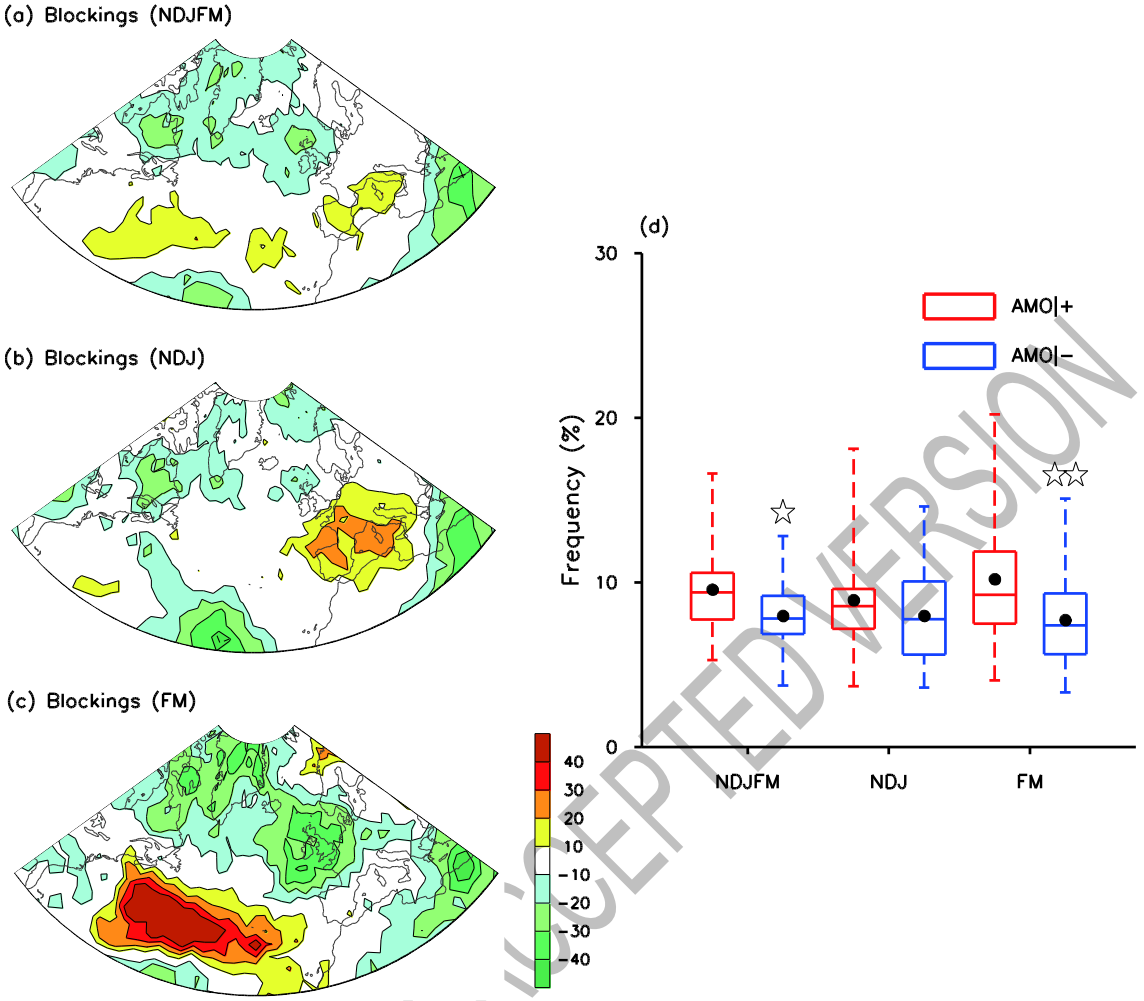

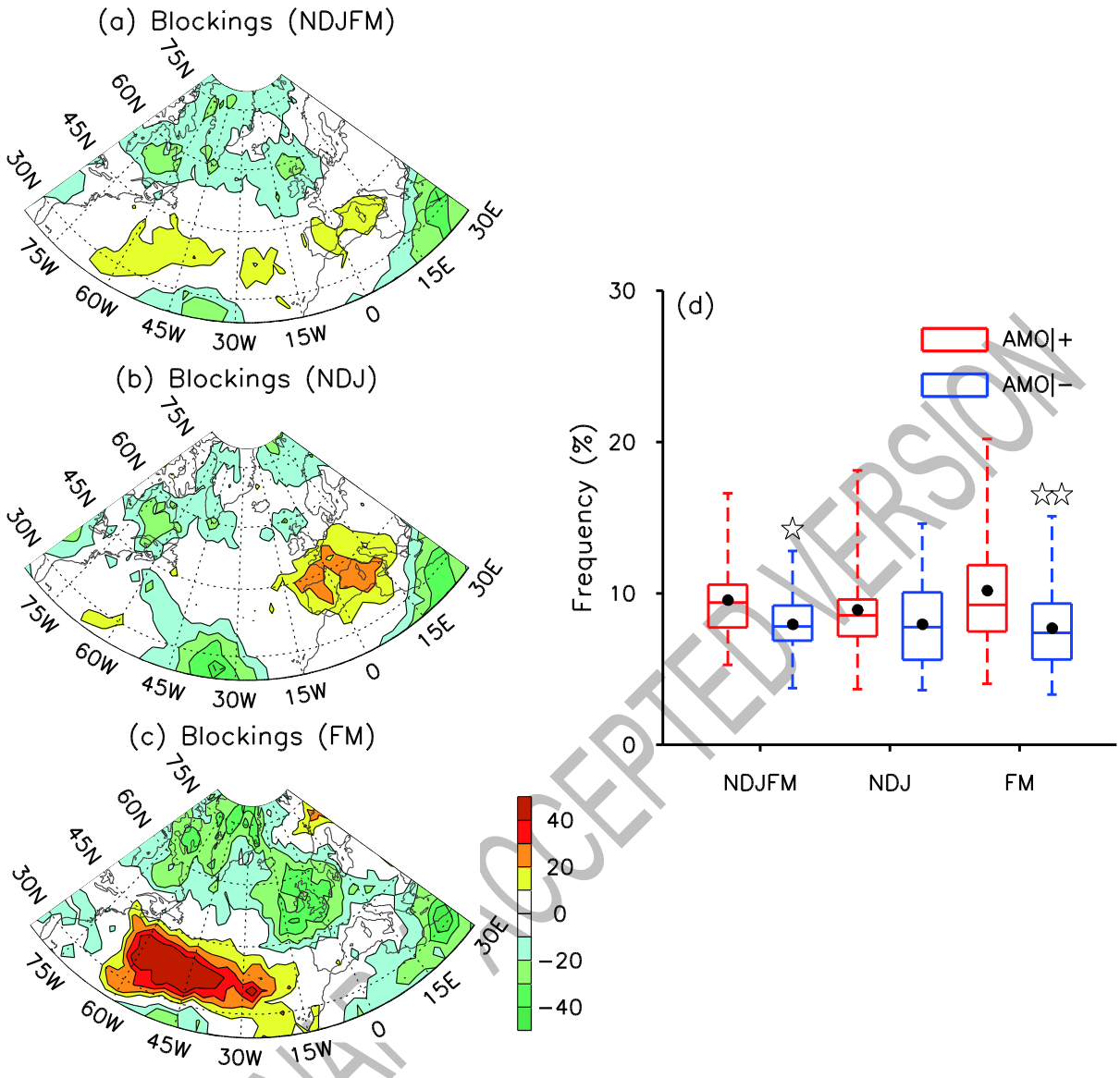

Fig. 9. Composite differences between AMO|− and AMO|+ years of the incidence of (a) November--March, (b) November--January and (c) February--March blocking highs (measured as the percentage relative to the blocking climatology during 1948--2011) restricted to the Euro-Atlantic sector (25°--80°N, 85°W--30°E). (d) Distribution of seasonal regime frequencies (40°--80°N, 85°W--30°E; measured as the ratio of the number of days when a certain grid point is blocked to the total number of days) in AMO|+ (red boxplots) and AMO|− (blue boxplots) for November--March, November--January and February--March. Boxplots indicate the maximum, upper-quartile, median, lower-quartile and minimum of the distribution

(horizontal bars). The mean of the distribution is shown by black diamonds, and asterisks indicate the significance level of the difference of the mean between AMO|− and AMO|+: one star, $p < 0.05$; two stars, $p < 0.01$.